





RESEARCH ARTICLE

Experimental coupling process efficiency and benefits of back surface reflectors in photovoltaic multi-junction photonic power converters

Esther Lopez^{1,2}  | Oliver Höhn¹  | Meike Schauerte¹ | David Lackner¹ | Michael Schachtner¹ | S. Kasimir Reichmuth¹  | Henning Helmers¹ 

¹III-V Photovoltaics and Concentrator Technology, Fraunhofer Institute for Solar Energy Systems ISE, Freiburg, Germany

²Now with: Instituto de Energía Solar, Universidad Politécnica de Madrid, Madrid, Spain

Correspondence

Henning Helmers, III-V Photovoltaics and Concentrator Technology, Fraunhofer Institute for Solar Energy Systems ISE, Freiburg, Germany.

Email: henning.helmerts@ise.fraunhofer.de

Funding information

Comunidad de Madrid, Grant/Award Number: 2019-T2/AMB-12959; German Federal Ministry of Education and Research (BMBF), Grant/Award Number: 16ES0788

Abstract

Current matching is crucial to maximize the efficiency of two-terminal multi-junction photovoltaic devices. However, even in perfectly designed devices, deviation from the target operating temperature and consequent changes in the subcell absorptances causes current mismatch between the subcell currents even at constant spectral conditions. Fortunately, luminescence coupling from current-overproducing subcells to current limiting subcells mitigates this effect. In this work, the coupling process efficiency in three-junction photonic power converters based on GaAs/AlGaAs rear hetero-junction subcells is experimentally quantified. A coupling process efficiency of $32\% \pm 9\%$ from top and middle subcells to the limiting bottom subcell is found. Under constant monochromatic illumination, the observed coupling reduces the current mismatch, induced by raising the temperature from current matched conditions at 25°C to 70°C , from 4.4% to 1.6%. Furthermore, in this work, three-junction photonic power converters with back surface reflectors are implemented. Those reflectors improve the device response at elevated temperatures by increasing the optical path length in the limiting subcell. It is shown experimentally how a back reflector effectively redirects photons that are emitted by the bottom subcell towards the upper subcells to reinforce luminescence coupling.

KEYWORDS

back surface reflector, current mismatch, III-V multi-junction cell, laser power converter, luminescence coupling, photonic power converter, temperature dependence

1 | INTRODUCTION

Photovoltaic (PV) cells can be used as light receivers, also called laser power converters or photonic power converters (PPC), in optical power transmission systems that supply power to remote loads. Application examples for this technology cover lightning safe structural health monitoring [1], high-voltage transmission line sensors [2], smart

implants [3], rotating systems [4], and others. To efficiently power downstream electronics, common voltages of 3.3 or 5 V are often desired. However, the photo voltage of the PV cell is usually much smaller than this (e.g., around 1 V for GaAs-based PV cells). Hence, either a DC/DC boost converter can be applied, as, for example, done in Ref. [5] or multiple subcells can be interconnected in series to multiply the voltage [6, 7]. Devices with integrated series connection on

This is an open access article under the terms of the Creative Commons Attribution License, which permits use, distribution and reproduction in any medium, provided the original work is properly cited.

© 2021 The Authors. Progress in Photovoltaics: Research and Applications published by John Wiley & Sons Ltd.

chip level can be realized following the well-known multi-junction [8] or multi-segment approach [9], or a combination of both [10]. In multi-junction PV cells the subcells are vertically stacked and series connected by tunnel diodes. Note that opposed to solar cells for multi-junction PPCs, the subcells are all based on the same absorber material tuned to the incident laser light [6, 7, 11–14]. In contrast, in multi-segment PV cells the subcells (also called segments) are laterally interconnected with a metal layer that connects the front side of one subcell with the rear side of the adjacent one. As the overall current in a series-connected device is limited by the subcell with the smallest current, in both configurations, ideally all series-connected subcells generate the same photo current (current match). In multi-segments cells this requires that all subcells need to be exposed to the same fraction of the light [15, 16]. However, in multi-junction cells all subcells need to absorb the same fraction of the incident light (assuming perfect collection of the photo-generated carriers). This means that for a PPC with N subcells, the subcell thicknesses must be carefully designed in a way that all subcells absorb just a fraction of $1/N$ of the light impinging of the device. Now, in real-world applications the operating conditions typically vary and, for example, temperature variations can cause current mismatch between the subcells even in a perfectly designed device [7, 13]. This reduces the output current and hence the conversion efficiency of the device.

In the case of multi-junction cells, current mismatch can be mitigated by luminescence coupling, between the subcells. Luminescence coupling originates from radiative recombination within the subcells. Under mismatch conditions the subcells with excess current are forward biased and operate at a voltage between maximum power point and open circuit voltage. Hence, radiative recombination of overproduced carriers emits photons close to the materials bandgap (luminescence spectrum) that can be re-absorbed in the same subcell (photon recycling) or in other subcells (luminescence coupling). Consequently, the overproduced photocurrent is partly redistributed among the other subcells. In the ideal case of purely radiative recombination (i.e., 100% radiative efficiency [17]) and complete absorption of the re-emitted photons in the other subcells (i.e., 100% luminescence coupling), eventually the mismatched device would become current matched due to this redistribution. Generally speaking, even though deviations from design conditions in temperature or, for example, in the illumination spectrum affect the subcells absorptance and thus cause current mismatch, luminescence coupling makes multi-junction cells less sensitive to it. In multi-junction solar cells the effects of luminescence coupling have been studied in a number of experimental and theoretical works [18–24]. In those devices, usually each subcell features a different bandgap, and therefore, luminescence coupling proceeds in only one direction (Figure 1 left), namely, from high to

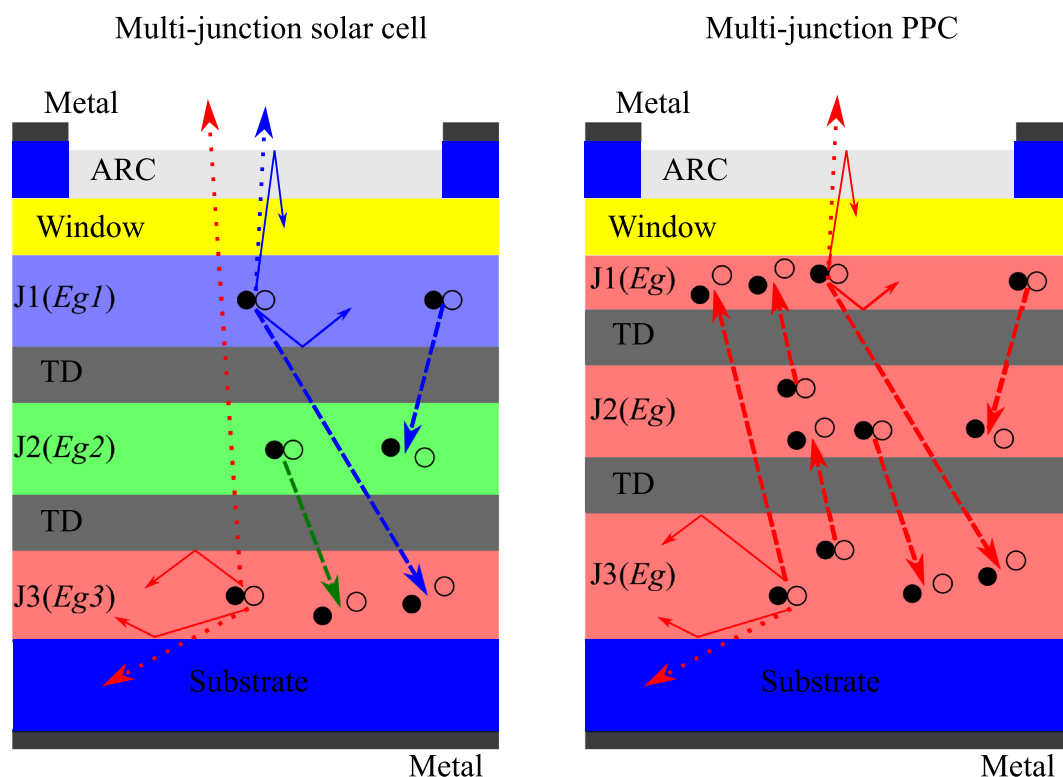


FIGURE 1 Sketches of a three-junction solar cell (with $E_{g1} > E_{g2} > E_{g3}$) (left) and a three-junction photonic power converter (right). Arrows represent luminescence photons (different colors means different photon energies). Photons involved in luminescence coupling are designated by dashed line arrows. The luminescence photons that escape through the front side or absorption into the substrate are designated by dotted line arrows. Photons that are trapped in each subcell as consequence of total internal reflection on interfaces with different refractive index are illustrated by the solid lines arrows [Colour figure can be viewed at wileyonlinelibrary.com]

low bandgap materials (i.e., from top to bottom subcells). In multi-junction PPCs, however, all subcells are usually made of the same material (Figure 1 right), so luminescence coupling can occur in both directions [12–14]. The fact that luminescence coupling is also possible towards upper subcells makes the presence of back surface reflectors (BSR) especially relevant to redirect those photons in multi-junction PPCs. In order to shed light on the operation of these devices, Wilkins et al. included luminescence coupling in drift-diffusion based simulations and predicted coupling efficiencies between the subcells [25]. However, to the best of our knowledge, coupling efficiencies so far have not been studied and quantified experimentally in real multi-junction PPC devices.

In this work the coupling process efficiency in three-junction PPCs based on GaAs is studied and quantified experimentally. It is derived from the measured spectral response (SR) under current mismatch conditions due to operation away from target wavelength or induced by high operating temperature (Section 3.1). Furthermore, for the first time, three-junction PPCs with BSR have been implemented (Section 2.1). The effects of those reflectors are analyzed in Section 3.2, where the SR of devices with and without reflectors is compared at different temperatures.

2 | DEVICES AND METHODS

2.1 | Devices

To study luminescence coupling effects, we analyze PPCs based on rear hetero-junctions, which provide elevated output voltages due to reduced diode saturation current which indicates more radiative devices [26, 27]. Three vertically stacked GaAs/Al_{0.30}Ga_{0.70}As rear hetero-junction subcells (J1, J2, and J3) are grown upright by metal-organic vapor phase epitaxy (MOVPE) on 4" p-type GaAs substrates. A sketch of the device structure is shown in Figure 1 (right). To avoid majority barriers at the GaAs/Al_{0.30}Ga_{0.70}As interface, the aluminum content is increased gradually. More details on this procedure can be found elsewhere [28, 29]. Each subcell is electrically passivated with a GaInP-based front surface field layer and an Al_{0.60}Ga_{0.40}As back surface field layer. Table 1 lists the subcell thicknesses, which provide current match at 25°C at two different wavelengths, 809 nm (Structure A) and 845 nm (Structure B), according to a transfer matrix model [30].

TABLE 1 Subcell thicknesses of Structures A and B, designed to provide current match at 25°C with 809 and 845 nm illumination, respectively

	Structure A (809 nm)	Structure B (845 nm)
Top subcell (J1)	308 nm	385 nm
Middle subcell (J2)	528 nm	670 nm
Bottom subcell (J3)	2650 nm	2650 nm

The 4" wafers with epitaxial Structures A and B are processed to PV cell devices with nominal designated areas of 1.001 cm² (later in this manuscript referred to as 1 cm² cells) and 0.054 cm² in the clean room laboratory at Fraunhofer ISE. Evaporated front metal contacts are used, resulting in a 0.5% grid coverage for 1 cm² cells used in measurements at low irradiance and 2% grid coverage for 0.054 cm² cells used in measurements at high irradiances. A two layer anti-reflection coating based on Ta₂O₅/MgF₂ (74/79 nm) is applied to minimize the reflectivity in the target wavelengths range (809 and 845 nm). As to the rear side, either a full area Pd/Zn/Pd/Au metallization for electrical contact is applied (PPCs processed on substrate) or a thin film process is conducted and a BSR is applied (PPCs processed on BSR) following the processing scheme described in detail in Ref. [29]. For the thin film process, first the front side is processed and then bonded to a temporal sapphire carrier. Subsequently, the GaAs substrate is wet chemically removed with NH₄:H₂O₂:H₂O. This etching stops at a GaInP-based etch stop layer, which is subsequently removed with a hydrochloride dip. Then, 99.1% of the now exposed back surface area is coated with 200 nm thermally evaporated gold, whereas the remaining 0.9% is used to provide low ohmic rear contact (with hundreds of point contacts of 10 μm diameter) by evaporation of a Pd/Zn/Pd/Au stack. Finally, a 30 μm copper layer is electroplated on the rear side to provide physical stabilization in addition to good electrical and thermal conductivity. As last step, the sapphire carrier is removed and flexible PV cell wafers with BSR on thin copper foil are obtained.

2.2 | Methods

External quantum efficiency (EQE) of the multi-junction device is measured with a LOANA solar cell analysis system at 25°C and 70°C on the 1 cm² PV cells with a minimal front metal grid coverage of 0.5% (to avoid measurement uncertainty due to shading effects). The monochromatic light used has a full width at half maximum (FWHM) of 8 nm and a wavelength accuracy of 1 nm. A transimpedance amplifier holds the solar cell at short circuit with remote sense. EQE measurements are conducted under different white bias light without spectral control, varying from no bias light to 0.3 suns according to the current generated in a calibrated Silicon-based monitor cell placed in the measurement plane. The 1 sun here means 1000 W/m² AM1.5 g like irradiance on a Silicon cell.

Furthermore, the spectral absorptances of the top, middle, and bottom subcells are modeled using the transfer matrix formalism [30], that is, purely optical consideration without accounting for luminescence coupling effects. For this purpose, the spectral optical data (absorption coefficient, refractive index) of the absorber layers (GaAs, n-doped 1×10^{17} cm⁻³) have been calibrated at 25°C and 70°C. If severe electrical losses such as significant surface recombination or significant bulk recombination due to insufficient diffusion length compared with the subcell thickness can be neglected, basically all of the generated minority carriers are collected, and thus, the absorptance equals the internal quantum efficiency. Consequently, the

simulated absorptance has been matched to measured internal quantum efficiency data of three isotype single-junction cells of different thickness (GaAs absorber layer thicknesses of 143, 261, and 447 nm). It is noted that the obtained GaAs optical data mostly agree well with literature data [31] but differs close to the bandgap above 840 nm, presumably because the optical bandgap is affected by the doping [32].

Current-voltage (*I*-*V*) characteristics are measured on 0.054 cm² concentration PV cells at different irradiances under a pulsed laser source (pulse duration of 4 ms to minimize heating of the device under test) with 809 nm center wavelength and a FWHM of 3 nm. The data are used to determine intensity-dependent spectral response (*SR*) at the laser wavelength. The laser is temperature controlled and calibrated to maintain its emission wavelengths for all studied irradiance levels. The laser beam is homogenized by two micro lens arrays to a square spot of 3.5 × 3.5 mm² (larger than the area of the measured cell), with a spatial uniformity of 98.8%. More details about the spatial light intensity uniformity in the test plane can be found in Ref. [33]. The temperature of the multi-junction PPCs is defined at 25°C or 70°C using a temperature controlled measurement chuck. The measurement procedure is as follows: The laser pulse is manually started, then after about 2 ms a voltage sweep is triggered which lasts for about 1 ms. During the sweep, the *I*-*V* characteristic is measured via 4-point technique using a calibrated resistor, a bipolar amplifier, and a high-speed transient recorder. A fraction of about 5% of the laser light is coupled to a calibrated GaAs-based monitor cell using a beam sampler. The current of the monitor cell is recorded during each *I*-*V* measurement to detect and compensate for small irradiance variations during the laser pulse: The measured current of the device under test is corrected according to the superposition principle, and fluctuations in the raw signal are reduced to deviations ≤ ±0.16% during one laser pulse [33]. Note that this procedure to compensate small irradiance variations is only valid when the current generated by the device under study is linear with irradiance. Rigorously, this is not the case in multi-junction devices, where luminescence coupling occurs. However, as the laser intensity fluctuations are small compared with the signal itself, the influence of luminescence coupling on the correction procedure is neglected. In order to determine the absolute irradiance in the test plane (*G*_{in}) at different laser intensities, a calibrated GaAs-based single-junction reference cell is used. The *I*-*V* curve of the reference cell is measured before and after measuring all the devices under test at each intensity. Again, the monitor cell current is used to detect and compensate for irradiance variations between the reference cell measurement and the multi-junction measurements.

In addition to wafer-level measurements on a temperature controlled chuck (25°C to 70°C), temperature-dependent *I*-*V* measurements over a broad range from 150 to 420 K are conducted using an evacuated cryostat chamber. For the latter, specimens mounted on planar copper submounts were prepared. Further details on the temperature-dependent *I*-*V* measurements with the laser set-up can be found in Ref. [13].

2.3 | Coupling process efficiency

In this work we introduce the coupling process efficiency (η_C) as the effective efficiency of redistributing the photocurrent under mismatched conditions from current-overproducing subcells to the current limiting subcell. It includes all losses in the coupling process within the multi-junction semiconductor structure, and it can be determined experimentally without knowledge about the actual number of photons emitted from each individual subcell. Note that this definition differs from the “total coupling efficiency” defined in Ref. [25], which describes per subcell the probability for photons emitted by radiative recombination from that subcell to be re-absorbed in any of the other junctions. The coupling process efficiency η_C is

$$\eta_C = \eta_{lum} \cdot \eta_{abs} \cdot \eta_{col} \quad (1)$$

where η_{lum} is the probability that excess carriers recombine radiatively and emit photons which escape the subcell where they are generated, reaching another subcell where they can be absorbed; η_{abs} is the probability to absorb photons generated by luminescence in another subcell and subsequent hole-electron pair generation; η_{col} is the probability of collecting the corresponding minority carriers. The impact of different coupling process efficiencies on the current density-voltage (*J*-*V*) characteristic of a three-junction PPC is illustrated in Figure 2. The excess carriers in two overproducing subcells recombine as consequence of the series connection imposed. This is illustrated in Figure 2 by arrows labeled as R_1 and R_2 , which represent the reduction in current from the photogenerated current to the current of the operating point. Depending on the material quality and its radiative efficiency, part of this recombination results in photons that can be re-absorbed in the limiting subcell and in turn raise its current. The gain in current in the limiting subcell (illustrated in Figure 2 by the arrow labeled as G) effectively raises the device current in dependence of the luminescence coupling process efficiency η_C .

Referring to the nomenclature of Figure 2, the coupling process efficiency can be expressed as follows:

$$\eta_C = \frac{G}{R_1 + R_2} \quad (2)$$

where the values for G , R_1 , and R_2 will depend on η_{lum} , η_{abs} , and η_{col} corresponding to the specific case under study (direction of luminescence propagation and features of the subcells involved). Equation 2 can be reformulated if the reduction in the current produced by the limiting subcell (D_3) equals the excess of generation in the overproducing subcells (D_1 and D_2), which means that $D_3 = D_1 + D_2$. Then

$$\eta_C = \frac{G}{(D_1 + D_3 - G) + (D_2 + D_3 - G)} = \frac{G}{3D_3 - 2G} \quad (3)$$

It is remarked that in fact coupling takes place in all directions; that is, overproducing subcells couple into all other subcells. However, in the end, for the question of overall current mismatch only the coupling

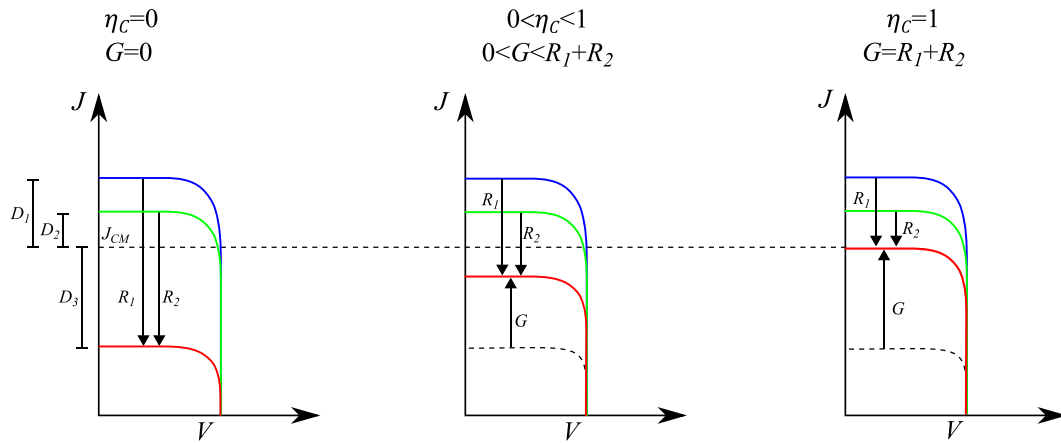


FIGURE 2 Illustration of the current density-voltage (J - V) characteristic of each subcell in a three-junction photonic power converter for a scenario where one subcell limits the device current, whereas the other two subcells have an excess current. The dashed line represents the average subcell current density, which would be the device current density in a current matched scenario (J_{CM}). The absolute difference between J_{CM} and the current density photogenerated by the subcells is denoted by D_1 , D_2 , and D_3 . In the overproducing subcells, the reduction from the photogenerated current density to the current density of the operating point is denoted by R_1 and R_2 . The gain in current density of the limiting subcell as consequence of coupling process is denoted by G . Three cases are shown where coupling process efficiencies increase from left (no coupling: $\eta_c = 0$) to right (perfect coupling: $\eta_c = 1$). Note that for the sake of simplicity, the open-circuit voltage of the subcells in this illustration is kept constant; more accurately, it would be influenced by the photogenerated current according to the diode model [Colour figure can be viewed at wileyonlinelibrary.com]

into the limiting subcell is relevant and empirically accessible with the approach taken in this study.

3 | RESULTS AND DISCUSSION

3.1 | Luminescence coupling

Luminescence coupling improves the performance of multi-junction PPCs by increasing the output current under current mismatch conditions. In order to analyze this phenomenon experimentally, the following points need to be addressed: (1) identify current mismatch conditions where luminescence coupling can appear, (2) determine the limiting current without luminescence coupling, and (3) determine how much this current increases due to the luminescence coupling effect. The key task is (2), because luminescence coupling between subcells is unavoidable under current mismatch conditions but to an unknown extent. However, as non-radiative recombination saturates with increasing irradiance, at low irradiances radiative recombination is considered to be less dominant and, hence, luminescence coupling less strong. Examples of measurements obtained at low irradiances are the EQE measurements shown in this section.

Figure 3 shows the effect of increasing bias illumination on the measured EQE for three cases: first, the reference case of Structure A measured at 25°C (target current match at 809 nm), second, the same structure but at elevated temperature of 70°C, and third, Structure B measured at 25°C (target current match at 845 nm), in all cases for samples processed on substrates, that is, without BSR. In addition, Figure 3 shows the modeled absorptances of the top, middle, and bottom subcells. Their intersection determines the current matching

wavelength: 809 and 819 nm for Structure A at 25°C and 70°C, respectively, and 845 nm for Structure B at 25°C. As can be seen in Figure 3, for all cases the bias-dependent measured EQE curves all intersect at the current matching wavelength expected from modeled absorptances. Now, when no luminescence coupling is present, we would expect the EQE to be determined by the minimum of the modeled absorptances as the current limiting subcell. On the contrary, in the measurements, we observe something else: When moving away from the intersection point, the measured EQE without bias light (0 suns), that is, at lowest irradiance and thus with minimal luminescence coupling, lies clearly above the minimum of the modeled subcells absorptances. At short (long) wavelengths the measured EQE is significantly higher than the absorptance of the bottom (top) subcell, which is the subcell with the lowest absorptance and thus limiting current at those wavelengths. With increasing bias light irradiance up to 0.04 suns, however, the measured EQE approaches the modeled absorptance of the bottom subcell, which is the subcell that receives the least of the broad band bias light and, thus, limits the current. For bias light irradiances above 0.04 suns, the measured EQE increases again and moves away from the simulated absorptance for wavelengths below the current matching one, where the bottom subcell limits the current generated not only by the bias light but also by the monochromator light.

Note that the use of different white bias light conditions changes the operating point of the subcells and the luminescence coupling intensity from one EQE curve to another, regardless which subcell is limiting the continuous current generated by the bias light. So the only way to obtain a constant EQE at one specific wavelength is when this wavelength corresponds to the current matching one and there is no luminescence coupling associated to the monochromatic illumination.

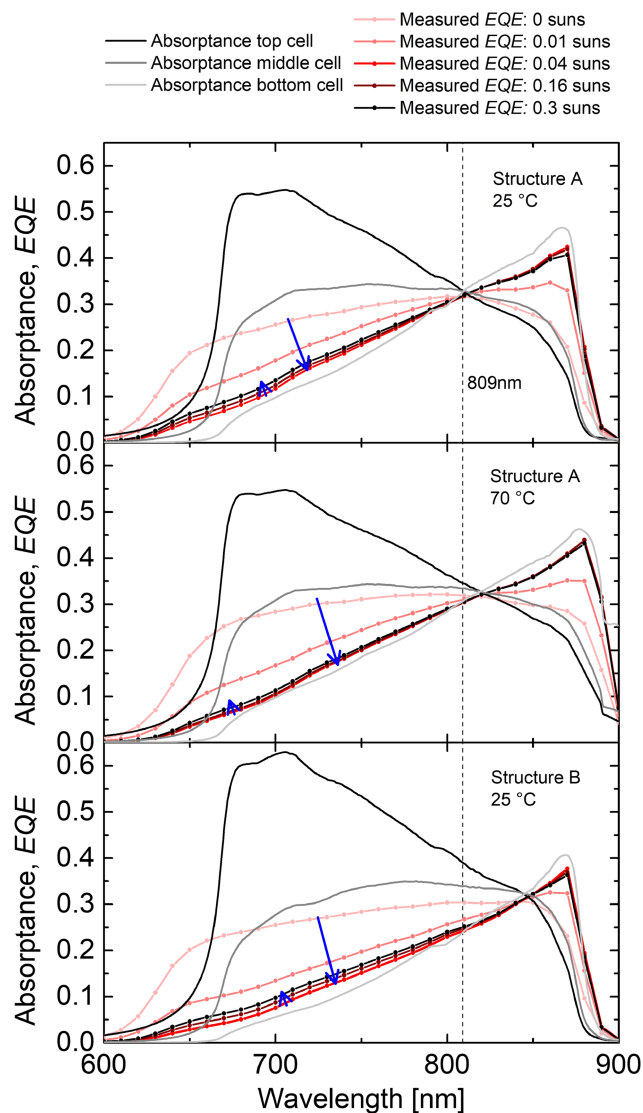


FIGURE 3 Measured bias light dependencies of three-junction photonic power converter EQEs for three cases: Structure A at 25°C (top), Structure A at 70°C (middle), and Structure B at 25°C (bottom). The spectrum of the white bias light used in the commercial setup is not under control, producing a continuous current that is limited by the bottom subcell when EQEs is measured under 0.01–0.3 suns. Blue arrows indicate the bias dependence of the EQE curves for 0–0.04 suns (right arrow) and 0.04–0.3 suns (left arrow). The modeled absorbances of top, middle, and bottom subcells are plotted as reference. Note that given the three-junction nature of the investigated device, the ideal value for both the modeled absorbance and the EQE at the current matching point would be 1/3. For a later discussion, the laser wavelength 809 nm is marked with a dashed line [Colour figure can be viewed at wileyonlinelibrary.com]

For this reason, we can consider that our optical model describes the real devices well, because at the expected current matching wavelength the EQE is independent of the white bias light (all EQE curves intersect), as expected from current match conditions where there is no luminescence coupling. However, the measured EQE without bias light (0 suns) deviates significantly from the model, where the EQE should follow the minimum of the modeled subcell absorbances. Two

different phenomena may cause such deviations: luminescence coupling from overproducing subcells and parallel resistance artifacts caused by non-infinite parallel resistance which lead to a higher output current from the limiting subcell when it operates at reverse voltages as consequence of the series connection. Both effects have been observed in multi-junction cells of GaAs similar to the ones studied here [12, 33]. These effects feature different bias light dependences: whereas the parallel resistances artifact diminishes with increasing bias light intensity and thus current density, the luminescence coupling effect intensifies with increasing intensity because the device becomes more radiative. Hence, we conclude that parallel resistance affects the EQE for bias light intensities below 0.04 suns. At higher intensities the effect of luminescence coupling becomes apparent. As the EQE measurement with a 0.04 suns bias approaches the modeled bottom subcell absorbance best, we consider this measurement to be least affected by luminescence coupling and parallel resistance artifacts. Note that a similar study was done in Ref. [35], where the optimal bias light intensity to minimize the EQE measurement artifact results also from the trade-off between the shunt and the luminescence coupling effects.

Figure 3 shows that only Structure A measured at 25°C provides current matching at 809 nm (Figure 3 top), which is the wavelength of our laser setup described in Section 2.2. Heating this structure to 70°C (Figure 3 middle) leads to a drop in the bandgap of the GaAs absorber layer and increase in the absorption coefficient at 809 nm. As a result, the top and middle subcells absorb more light under laser illumination, leaving a lower fraction of the incident light to be absorbed by the bottom subcell [7]. For that reason the intersection point in the EQE curves shifts towards higher wavelengths to 819 nm. Structure B measured at 25°C (Figure 3 bottom) provides current matching at 845 nm (cf. Table 1). Hence, two current mismatched structures at a wavelength of 809 nm are identified: Structure A at 70°C and Structure B at 25°C.

The SR in absence of luminescence coupling for Structure A at 70°C and Structure B at 25°C can be estimated with the EQE measurements with 0.04 suns bias light. To this end, we impose that the relative reduction in the EQE at 809 nm respect to the one obtained under current match conditions must be the same than the relative reduction in the SR derived from *I-V* measurements under illumination with a 809 nm laser. The SR in absence of luminescence coupling for Structure A at 70°C and Structure B at 25°C is estimated and plotted in Figure 4 (red and blue star respectively), using as reference the SR obtained under current match conditions (Structure A at 25°C) and maximum irradiance. Note that whereas EQE is measured on cells with a minimal front metal grid coverage (0.5%), the power-dependent SR derived from laser *I-V* measurements is measured on cells with a denser metal grid (2%) of the same wafer. As mentioned before, luminescence coupling between subcells is unavoidable under current mismatch conditions, so it is not possible to measure SR with total absence of this effect. However, at the irradiance with only 0.04 suns bias light, the injection level of ~ 0.35 mA/cm² is assumed to be so low that luminescence coupling is very weak (quite below 1%) and this effect can be well neglected. Note that this assumption leads to a

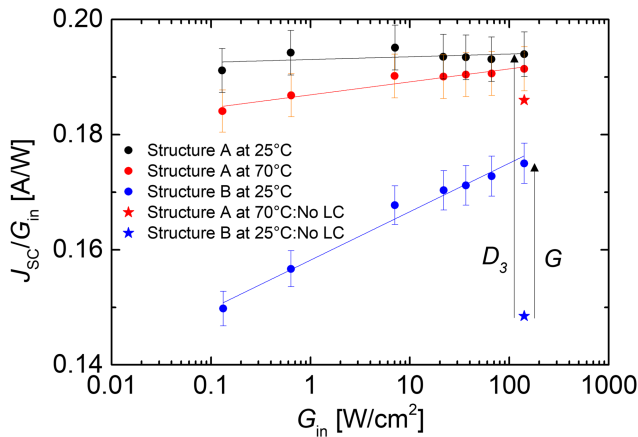


FIGURE 4 Measured spectral response at 809 nm derived from short-circuit current density (J_{SC}) divided by monochromatic irradiance (G_{in}). Stars represent the estimated value in absence of luminescence coupling, using as reference the SR obtained under current match conditions (Structure A at 25°C) and maximum irradiance. Error bars correspond to variations in the SR caused by wavelength variation in the laser emission ($\pm 2\%$) [Colour figure can be viewed at wileyonlinelibrary.com]

slight underestimation in the experimentally derived coupling process efficiency.

Figure 4 shows the measured irradiance-dependent SR of Structure A (at 25°C and 70°C) and Structure B (at 25°C) for the illumination by a laser with 809 nm wavelength. The current matched device (Structure A at 25°C, black circles) shows the highest SR. Within the measurement uncertainty it is independent of irradiance, as expected for this case without luminescence coupling. For the same device but at elevated temperature of 70°C (red circles) the measured SR is reduced and a minor increase with irradiance is observed (1.2% increase in SR per irradiance decade). A similar but much more pronounced trend is observed in Structure B measured at 25°C (5.3% increase in SR per irradiance decade), which is strongly current mismatched under 809 nm laser light. The increase in SR with irradiance is caused by luminescence coupling, as the subcells become more and more radiative as irradiance increases [13].

In the current mismatch cases evaluated in Figure 4 (red and blue points) the excess current of the top and the middle subcells radiatively couples into the bottom subcell. The efficiency of this process can be calculated with Equation 3, using the parameters G and D_3 illustrated in Figure 2. In this case, G is the increase in the limiting current caused by the luminescence coupling from top and middle subcells, and D_3 is the difference between the current produced by the limiting bottom subcell and the ideal current match, as consequence of an excess of generation in the top and middle subcells. Therefore, G is determined as the difference between the SR without luminescence coupling (blue/red star) and the measured SR (blue/red dots), and D_3 as the difference between the SR without luminescence coupling (blue/red star) and the SR obtained for current match conditions (black dots). With those values, a coupling process efficiency of $32\% \pm 9\%$ is obtained for the Structure B at 25°C, for the highest irradiance provided by the 809 nm laser ($G_{in} = 140 \text{ W/cm}^2$). The

uncertainty in the coupling process efficiency is calculated according to the law for the propagation of uncertainty [36, 37], including variations in the SR caused by wavelength variation in the laser emission ($\pm 2\%$) and non-perfect current matching of the Structure A at 25°C and 809 nm (0.4%). The latter is obtained from the non-perfect intersection of all EQE curves in Figure 3 (top). For the highest irradiance, the coupling process efficiency reduces the temperature-induced current mismatch from 4.4% (without luminescence coupling) to 1.6%, when increasing temperature in Structure A from 25°C to 70°C. This 1.6% reduction in SR is within the error bars that correspond to variations in the SR caused by wavelength variation in the laser emission ($\pm 2\%$). A 32% of the excess current in top and middle subcells is coupled to the bottom subcell. This value is expected to be mainly determined by η_{lum} in Equation 1. Since according to results obtained in single-junction cells with the same structure as the bottom subcell (without BSR), η_{col} is expected to be close to 100%, whereas η_{abs} is expected to be around 80% for the emitted photon energies close to the GaAs bandgap [29]. In the current mismatch cases analyzed in this section, η_{lum} is the probability that excess carriers in the top and middle subcells recombine radiatively and emit photons which escape these subcells to be absorbed in the bottom subcell. Due to the thin thickness of the top and middle subcells, η_{lum} can be analyzed like an external luminescence efficiency emitted from a thin semiconductor heterostructure, like the ones studied in Ref. [38], but considering the photons that escape through the back side, not through the front side. This parameter is very sensitive to small non-radiative and parasitic optical losses, such as free carrier absorption in highly doped semiconductor layers, so even with highly radiative subcells we can obtain relatively small η_{lum} , compared with the internal radiative efficiency. To identify if η_{lum} is dominated by non-radiative losses or parasitic optical losses, a similar study to the one reported in Ref. [38] should be done in the future.

3.2 | Impact of the BSR

The implementation of BSRs in single-junction and multi-junction PV cells has been studied for solar and thermophotovoltaic applications [29, 39–41]. However, to the best of our knowledge, these reflectors have not been implemented in multi-junction PPCs based on one absorber material yet. In order to analyze the impact of a BSR in the performance of these devices, two cells with Structure A (current match at 809 nm and 25°C) are compared: one processed on substrate, the other processed as thin film cell with a gold BSR. The presence of the gold BSR increases the open-circuit voltage of the PPC by 18 mV, due to photon recycling, that is, a reduction of the dark saturation current in the bottom subcell [29, 42]. In addition, in the multi-junction case the BSR also impacts luminescence coupling between the subcells and thus the output current of the device in current mismatched conditions. This effect will be analyzed in more detail in the following.

Figure 5 shows the measured irradiance-dependent SR of Structure A with and without BSR for the illumination by a laser with

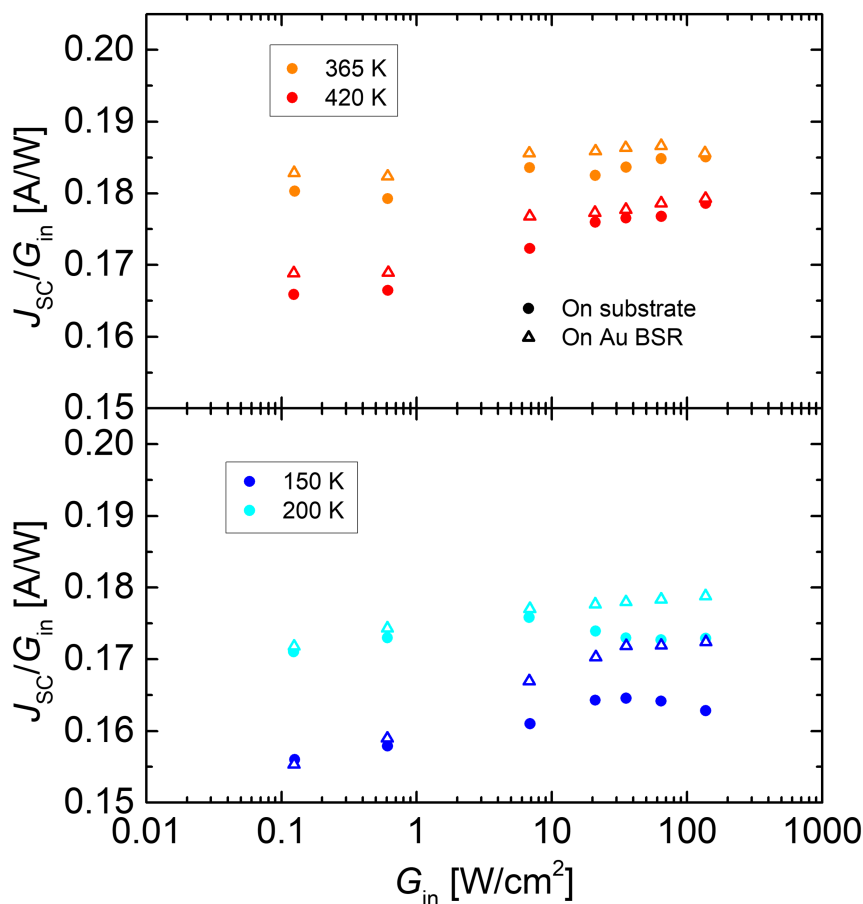


FIGURE 5 Measured spectral response of multi-junction cells with Structure A derived from short-circuit current density (J_{SC}) divided by monochromatic irradiance (G_{in}) from a 809 nm laser. Measurements are carried out for cells on substrate and cells on Au BSR. The top and bottom graphs show the measured data at high and low temperatures, respectively, where the bottom and top cells, respectively, limit the output current [Colour figure can be viewed at wileyonlinelibrary.com]

809 nm wavelength. In the top (bottom) graph the SR measured above (below) 25°C is plotted. At temperatures above 25°C shown in the top of Figure 5, the SR increases with the irradiance. The presence of a BSR contributes to increase the SR, but this increase does not change with G_{in} . At temperatures below 25°C shown in the bottom of Figure 5, for the multi-junction PPC processed on a substrate, two regimes can be identified: the first regime, at low irradiances (below ~ 10 W/cm²), where the SR increases with G_{in} , and the second regime, at high irradiances (above ~ 10 W/cm²), where SR is clearly saturated and does not increase with G_{in} . The first regime is not affected by the presence of a BSR, whereas in the second regime the BSR significantly increases the SR of the cell. This increase in SR is most pronounced at lowest temperature (150 K), and it is intensified with increasing G_{in} .

At temperatures above 25°C (Figure 5 top), when the bottom subcell is limiting the output current, the SR increases with the irradiance for the same reasons explained in Section 3.1: luminescence coupling from the top and the middle subcells to the bottom one. Under these circumstances, the presence of the Au BSR increases the SR. However, this increase is not intensified with the irradiance (G_{in}), which indicates that it is not related to luminescence coupling. The SR increase can be understood from the increased optical path for incident photons in the current limiting bottom subcell. The coupling process efficiency from top to bottom subcells, however, is not affected because, as mentioned in Section 3.1, this is dominated by η_{lum} in the

upper two subcells. This η_{lum} is not affected by a BSR, but by the radiative efficiency of the top and the middle subcells and the redirection of luminescence photons towards the bottom subcell, as consequence of a narrow escape cone at the front surface (cf. illustration in Figure 1) [19, 38].

However, the presence of a BSR can improve significantly the η_{lum} in the bottom subcell. A BSR makes it possible to redirect an important fraction of the photons emitted by the bottom subcell that otherwise would be lost in the substrate (illustrated in Figure 1). So those photons can reach upper subcells and be absorbed there. This is why at temperatures below 25°C (Figure 5 bottom), when the top subcell is limiting the SR, the cell with a BSR increases its SR in respect to the cell without BSR at irradiances above ~ 10 W/cm². At lower irradiances, the increase in SR with G_{in} is not affected by the presence of a BSR, which indicates that the luminescence generating this increase does not originate from the bottom subcell but from the middle one. Here, the coupling process efficiency cannot be quantified, because the considerations used to obtain Equation 3 are not fulfilled in this case: The current in the limiting top subcell is reduced with respect to the current match value due to insufficient absorption and that cannot be compensated by absorption in the other subcells, so $D_3 \neq D_1 + D_2$. However, the results shown in Figure 5 show the influence of a BSR on luminescence coupling from the bottom to the top subcells in a three-junction PPC.

4 | CONCLUSIONS

In this work a methodology has been presented to assess the coupling process efficiency in multi-junction PV cells based on one absorber material only, as used in photonic power converters for one monochromatic wavelength. The procedure is based, on one hand, on absorptance modeling and measurements at low irradiance conditions (bias-dependent EQE) to estimate the spectral response in absence of luminescence coupling at a target wavelength. On the other hand, the procedure also requires measurements at high irradiance conditions, like *I*-*V* measurements under high-power laser illumination to quantify the coupling process efficiency under current mismatch conditions. For photonic power converters based on three stacked GaAs/AlGaAs rear hetero-junctions, the coupling process efficiency has been experimentally quantified and shown to be $32\% \pm 9\%$ at 140 W/cm^2 illumination (809 nm) for coupling from the upper two subcells to the limiting bottom subcell. This high coupling process efficiency reduces the temperature-induced current mismatch when increasing temperature from 25°C to 70°C from 4.4% without luminescence coupling to 1.6%. Besides, it is shown how implementation of a BSR can increase the spectral response at high temperatures, as the absorptance in the current limiting bottom subcell increases due to an increased optical path. Furthermore, at low temperatures, such a reflector facilitates luminescence coupling from the overproducing bottom subcell towards the top and middle subcells, as it redirects photons that would otherwise be lost in the substrate.

ACKNOWLEDGEMENTS

The authors wish to thank Jochen Markert for epitaxial growth of the semiconductor structures; Gabriele Mikolasch for electroplating support; Alexander Wekkeli, Elvira Fehrenbacher, and Elisabeth Schäffer for measurement support; and Eduard Oliva, Felix Predan, Gerald Siefer, and Frank Dimroth for many valuable discussions. This work was partly funded by the German Federal Ministry of Education and Research (BMBF) through the project "Lightbridge" (16ES0788). Esther López acknowledges an Atracción del Talento Fellowship (2019-T2/AMB-12959) funded by the Comunidad de Madrid.

ORCID

Esther Lopez  <https://orcid.org/0000-0003-4256-9329>

Oliver Höhn  <https://orcid.org/0000-0002-5991-2878>

S. Kasimir Reichmuth  <https://orcid.org/0000-0002-4963-0236>

Henning Helmers  <https://orcid.org/0000-0003-1660-7651>

REFERENCES

- Worms K, Klamouris C, Wegh F, et al. Reliable and lightning-safe monitoring of wind turbine rotor blades using optically powered sensors. *Wind Energy*. 2017;20(2):345-360. <https://doi.org/10.1002/we.2009>
- de Nazare FVB, Werneck MM. Hybrid optoelectronic sensor for current and temperature monitoring in overhead transmission lines. *IEEE Sens J*. 2012;12(5):1193-1194. <https://doi.org/10.1109/JSEN.2011.2163709>
- Park S, Borton DA, Kang M, Nurmikko AV, Song Y-K. An implantable neural sensing microsystem with fiber-optic data transmission and power delivery. *Sensors*. 2013;13(5):6014-6031. <https://doi.org/10.3390/s130506014>
- Spillman WB, Crowne DH, Woodward DW. Optically powered and interrogated rotary position sensor for aircraft engine control applications. *Opt Lasers Eng*. 1992;16(2):105-118. [https://doi.org/10.1016/0143-8166\(92\)90003-P](https://doi.org/10.1016/0143-8166(92)90003-P)
- Helmers H, Armbruster C, von Ravenstein M, Derix D, Schöner C. 6-W optical power link with integrated optical data transmission. *IEEE Trans Power Electron*. Aug. 2020;35(8):7904-7909. <https://doi.org/10.1109/TPEL.2020.2967475>
- Schubert J, Oliva E, Dimroth F, Guter W, Loeckenhoff R, Bett AW. High-voltage GaAs photovoltaic laser power converters. *IEEE Trans Electron Devices*. Feb. 2009;56(2):170-175. <https://doi.org/10.1109/TED.2008.2010603>
- Helmers H, Wagner L, Garza CE, et al. Photovoltaic cells with increased voltage output for optical power supply of sensor electronics. *Proc Sens*. 2015;519-524. <https://doi.org/10.5162/sensor2015/D1.4>
- Friedman DJ, Olson JM, Kurtz S. High-efficiency III-V multijunction solar cells. In: *Handbook of Photovoltaic Science and Engineering*. Chichester, West Sussex: John Wiley & Sons, Ltd; 2011:314-364.
- Datas A, Linares PG. Monolithic interconnected modules (MIM) for high irradiance photovoltaic energy conversion: a comprehensive review. *Renew Sustain Energy Rev*. 2017;73:477-495. <https://doi.org/10.1016/j.rser.2017.01.071>
- Wagner L, Reichmuth SK, Philipps SP, Oliva E, Bett AW, Helmers H. Integrated series/parallel connection for photovoltaic laser power converters with optimized current matching. *Prog Photovolt*. 2020. <https://doi.org/10.1002/pip.3353>
- Fafard S, Proulx F, York MC, et al. High-photovoltage GaAs vertical epitaxial monolithic heterostructures with 20 thin p/n junctions and a conversion efficiency of 60%. *Appl Phys Lett*. 2016;109(13):131107. <https://doi.org/10.1063/1.4964120>
- Fafard S, York MC, Proulx F, et al. Ultrahigh efficiencies in vertical epitaxial heterostructure architectures. *Appl Phys Lett*. 2016;108(7):071101. <https://doi.org/10.1063/1.4941240>
- Reichmuth SK, Helmers H, Philipps SP, Schachtner M, Siefert G, Bett AW. On the temperature dependence of dual-junction laser power converters. *Prog Photovolt Res Appl*. 2017;25(1):67-75. <https://doi.org/10.1002/pip.2814>
- Proulx F, York MC, Provost PO, et al. Measurement of strong photon recycling in ultra-thin GaAs n/p junctions monolithically integrated in high-photovoltage vertical epitaxial heterostructure architectures with conversion efficiencies exceeding 60%. *Phys Status Solidi RRL - Rapid Res Lett*. 2017;11(2):1600385. <https://doi.org/10.1002/pssr.201600385>
- Wagner L, Bett AW, Helmers H. On the alignment tolerance of photovoltaic laser power converters. *Optik*. 2017;131:287-291. <https://doi.org/10.1016/j.ijleo.2016.11.072>
- Kimovec R, Helmers H, Bett AW, Topić M. Power loss mechanisms in small area monolithic-interconnected photovoltaic modules. *Opto-Electron Rev*. 2018;26(2):158-164. <https://doi.org/10.1016/j.opelre.2018.04.002>
- Green MA. Radiative efficiency of state-of-the-art photovoltaic cells. *Prog Photovolt Res Appl*. 2012;20(4):472-476. <https://doi.org/10.1002/pip.1147>
- Tayagaki T, Reichmuth SK, Helmers H, Siefert G. Transient analysis of luminescent coupling effects in multi-junction solar cells. *J Appl Phys*. 2018;124(18):183103. <https://doi.org/10.1063/1.5046543>
- Walker AW, Höhn O, Micha DN, et al. Impact of photon recycling and luminescence coupling on III-V single and dual junction photovoltaic devices. *J Photonics Energy*. Jan. 2015;5(1):053087. <https://doi.org/10.1117/1.JPE.5.053087>

20. Lan D, Geisz JF, Steiner MA, Garcia I, Friedman DJ, Green MA. Improved modeling of photoluminescent and electroluminescent coupling in multijunction solar cells. *Sol Energy Mater sol Cells*. Dec. 2015; 143:48-51. <https://doi.org/10.1016/j.solmat.2015.06.036>
21. Steiner MA, Geisz JF, Moriarty TE, et al. Measuring IV Curves and Subcell Photocurrents in the Presence of Luminescent Coupling. *IEEE J Photovolt*. 2013;3(2):879-887. <http://doi.org/10.1109/jphotov.2012.2228298>
22. France RM, Geisz JF, Garcia I, et al. Quadruple-junction inverted metamorphic concentrator devices. *IEEE J Photovolt*. 2015;5(1):432-437. <https://doi.org/10.1109/JPHOTOV.2014.2364132>
23. Lan D, Green MA. Equivalent circuit analysis of radiative coupling in monolithic tandem solar cells. *Appl Phys Lett*. 2015;106(26):263902. <https://doi.org/10.1063/1.4923209>
24. Lan D, Green MA. Photoluminescent and electroluminescent couplings in monolithic tandem solar cells. *Prog Photovolt Res Appl*. 2016; 24(12):1566-1576. <https://doi.org/10.1002/pip.2750>
25. Wilkins M, Valdivia CE, Gabr AM, Masson D, Fafard S, Hinz K. Luminescent coupling in planar opto-electronic devices. *J Appl Phys*. 2015;118(14):143102. <https://doi.org/10.1063/1.4932660>
26. Ragay FW, Ruigrok EWM, Wolter JH. GaAs-AlGaAs heterojunction solar cells with increased open-circuit voltage, in *Proceedings of 1994 IEEE 1st World Conference on Photovoltaic Energy Conversion - WCPEC (A Joint Conference of PVSC, PVSEC and PSEC)*, Dec. 1994;2: 1934-1937 doi: <https://doi.org/10.1109/WCPEC.1994.520747>
27. Lumb MP, Steiner MA, Geisz JF, Walters RJ. Incorporating photon recycling into the analytical drift-diffusion model of high efficiency solar cells. *J Appl Phys*. 2014;116(19):194504. <https://doi.org/10.1063/1.4902320>
28. Hwang S-T, Kim S, Cheun H, et al. Bandgap grading and Al_{0.3}Ga_{0.7}As heterojunction emitter for highly efficient GaAs-based solar cells. *Sol Energy Mater sol Cells*. Oct. 2016;155:264-272. <https://doi.org/10.1016/j.solmat.2016.06.009>
29. Schilling CL, Hohn O, Micha DN, et al. Combining photon recycling and concentrated illumination in a GaAs heterojunction solar cell. *IEEE J Photovolt*. 2018;8(1):348-354. <https://doi.org/10.1109/JPHOTOV.2017.2777104>
30. Harbecke B. Coherent and incoherent reflection and transmission of multilayer structures. *Appl Phys B*. Mar. 1986;39(3):165-170. <https://doi.org/10.1007/BF00697414>
31. Levinshtein MEM, Rumyantsev S, Shur M (Eds). *Handbook Series on Semiconductor Parameters*. Singapore: World Scientific; 1996.
32. Erskine DJ, Taylor AJ, Tang CL. Dynamic Burstein-Moss shift in GaAs and GaAs/AlGaAs multiple quantum well structures. *Appl Phys Lett*. 1998;45(11):1209-1211. <https://doi.org/10.1063/1.95100>
33. Reichmuth SK, Helmers H, Garza CE, Vahle D, de Boer M, Stevens L, Mundus M, Bett AW, Siefer G. Transient I-V measurement set-up for photovoltaic laser power converters under monochromatic irradiance. In: *32nd European Photovoltaic Solar Energy Conference*. 2016;5-10. <https://doi.org/10.4229/EUPVSEC20162016-1AO.1.2>
34. Nakamoto T, Makita K, Tayagaki T, Aihara T, Okano Y, Sugaya T. Spectral response measurements of each subcell in monolithic triple-junction GaAs photovoltaic devices. *Appl Phys Express*. 2019;12(10): 102015. <https://doi.org/10.7567/1882-0786/ab45d8>
35. Li J-J, Lim SH, Allen CR, Ding D, Zhang Y-H. Combined effects of shunt and luminescence coupling on external quantum efficiency measurements of multijunction solar cells. *IEEE J Photovolt*. 2011;1(2): 225-230. <https://doi.org/10.1109/JPHOTOV.2011.2172188>
36. Clifford AA. *Multivariate Error Analysis: A Handbook of Error Propagation and Calculation in Many-Parameter Systems*. London: Applied Science Publishers; 1973.
37. *Guide to the Expression of Uncertainty in Measurement*. Geneva, Switzerland: Int. Org. Standardization; 1995.
38. Schnitzer I, Yablonovitch E, Caneau C, Gmitter TJ. Ultrahigh spontaneous emission quantum efficiency, 99.7% internally and 72% externally, from AlGaAs/GaAs/AlGaAs double heterostructures. *Appl Phys Lett*. 1993;62(2):131-133. <https://doi.org/10.1063/1.109348>
39. Kayes BM, Nie H, Twist R, Spruytte SG, Reinhardt F, Kizilyalli IC, Higashi GS. 27.6% Conversion efficiency, a new record for single-junction solar cells under 1 sun illumination, in *2011 37th IEEE Photovoltaic Specialists Conference*, 2011, pp. 4-8, <https://doi.org/10.1109/PVSC.2011.6185831>
40. Fan D, Burger T, McSherry S, Lee B, Lenert A, Forrest SR. Near-perfect photon utilization in an air-bridge thermophotovoltaic cell. *Nature*. 2020;586(7828):237-241. <https://doi.org/10.1038/s41586-020-2717-7>
41. Lan D, Green MA. The potential and design principle for next-generation spectrum-splitting photovoltaics: targeting 50% efficiency through built-in filters and generalization of concept. *Prog Photovolt Res Appl*. 2019;27(11):899-904. <https://doi.org/10.1002/pip.3081>
42. Miller OD, Yablonovitch E, Kurtz SR. Strong internal and external luminescence as solar cells approach the Shockley-Queisser limit. *IEEE J Photovolt*. Jul. 2012;2(3):303-311. <https://doi.org/10.1109/JPHOTOV.2012.2198434>

How to cite this article: Lopez E, Höhn O, Schauerte M, et al. Experimental coupling process efficiency and benefits of back surface reflectors in photovoltaic multi-junction photonic power converters. *Prog Photovolt Res Appl*. 2021;29:461-470. <https://doi.org/10.1002/pip.3391>